

Jet-Surface Interaction Test: Flow Measurement Results

Cliff Brown * and Mark Wernet †

NASA Glenn Research Center, Cleveland, OH, 44135, USA

Modern aircraft design often puts the engine exhaust in close proximity to the airframe surfaces. Aircraft noise prediction tools must continue to develop in order to meet the challenges these aircraft present. The Jet-Surface Interaction Tests have been conducted to provide a comprehensive quality set of experimental data suitable for development and validation of these exhaust noise prediction methods. Flow measurements have been acquired using streamwise and cross-stream particle image velocimetry (PIV) and fluctuating surface pressure data acquired using flush mounted pressure transducers near the surface trailing edge. These data combined with previously reported far-field and phased array noise measurements represent the first step toward the experimental data base. These flow data are particularly applicable to development of noise prediction methods which rely on computational fluid dynamics to uncover the flow physics. A representative sample of the large flow data set acquired is presented here to show how a surface near a jet affects the turbulent kinetic energy in the plume, the spatial relationship between the jet plume and surface needed to generate surface trailing-edge noise, and differences between heated and unheated jet flows with respect to surfaces.

Nomenclature

c_a	speed of sound at ambient conditions
c_j	speed of sound at jet exit conditions
D_j	jet exit diameter
h	radial distance from jet centerline to surface
M_a	acoustic Mach number ($M_a = U_j/c_a$)
M_j	gas dynamic jet Mach number ($M_j = U_j/c_j$)
r	radial distance to the jet centerline
TKE	turbulent kinetic energy
u, v, w	three components of fluctuating velocity
U_j	mean ideally expanded jet exit velocity
x	axial location relative to the jet exit plane
X_c	potential core length of the equivalent isolated jet
x_{PIV}	axial distance from the jet exit to PIV measurement plane
x_{TE}	axial distance from jet exit to surface trailing edge

I. Introduction

The design of many modern aircraft places the engine exhaust in close proximity to the airframe surfaces. Future designs of both subsonic¹ and supersonic² aircraft are likely to push the integration of propulsion and airframe even closer in search of greater aerodynamic efficiency and reduced noise. However, an effective design process requires an understanding of the parameter space in order to allow informed trade-offs between competing priorities. For example, increasing the engine bypass ratio may increase fuel efficiency

*Research Engineer, Acoustics Branch, 21000 Brookpark Rd., AIAA Member.

†Research Engineer, Optical Instrumentation and NDE Branch, 21000 Brookpark Rd., AIAA Senior Member.

but the larger diameter engine exhausts directly onto the wing adding a significant noise source. Jet-surface interaction tests have been supported by the NASA High Speed and Fixed Wing projects to address the class of problems that arise in such a scenario: when the engine exhaust interacts with an airframe surface to create a new source of noise or shield the existing engine exhaust noise from observers on the ground.

A system level study incorporating many aircraft components combines predictions of performance, efficiency, and noise until the optimal design is determined. However, the ability to predict the noise created or shielded when a high-speed engine exhaust interacts with an airframe surface has been, historically, limited. Furthermore, quality experimental data suitable for developing and validating engine noise prediction schemes that incorporate the nearby surfaces is usually based on a particular aircraft concept and, therefore, of limited use to other configurations and often proprietary. A series of tests at the NASA Aero-Acoustic Propulsion Laboratory were envisioned to fill this void by providing an high quality open set of experimental noise and flow data over a range of surface geometries, surface positions, and flow parameters to developers of aircraft noise prediction methods. These new tools could then feed noise predictions to the system level studies and allow a more informed optimization study. During phase one, the noise of a jet near a simple planar surface was measured to (1) validate existing engine exhaust noise prediction scheme in the presence of a surface and (2) to determine regions of interest for future testing.^{3,4} Particle Image Velocimetry (PIV) flow measurements were acquired in phase two at surface locations where, based on these prior noise measurements, the jet-surface interaction noise source was the dominate or the surface was only acting to shield the jet mixing noise. PIV data were also acquired in the transition region between these extreme points where the jet-surface interaction noise and jet mixing noise sources are nearly equal in strength. An analysis of these data showed some large changes to the flow properties between the first and second radial surface positions tested. Therefore, a second test was conducted to investigate the flow when a surface is moved in small increments near the nozzle lip. This additional test used a different nozzle profile (same exit diameter) mounted to a different jet rig allowing for some experimental validation of the PIV data set. Combined, these flow data are presented to facilitate development and validation of the Computational Fluid Dynamics (CFD) simulations that underlie many engine exhaust noise prediction methods.

Jet-surface interaction noise broadly describes an increase in low frequency noise that results when a hard surface is located near turbulent jet. This increase is generally attributed to two source mechanisms: flow 'scrubbing' noise and trailing edge 'scattering' noise. Flow scrubbing is created by the turbulent flow as it passes along the surface. Trailing edge noise, which is the dominant source in the configurations these there,^{3,4} is generated when the wall (surface) bounded flow passes over an edge and transitions to a free-shear flow. Thus, the flow velocity, turbulent kinetic energy (TKE), edge length covered by flow (wetted area), and fluctuating pressure near the edge are believed to be the key flow parameters governing the generation of trailing edge noise. In addition to the jet-surface interaction noise, noise is created turbulent mixing in the primary jet mixing region (opposite the surface) and in the secondary mixing region (downstream of the surface);⁵ certainly in the secondary mixing layer and possibly in the primary jet mixing layer, a surface very near the jet may have influence the turbulent kinetic energy and, therefore, the jet mixing noise. The PIV data presented show the velocity and TKE in each of these regions so that, when combined with published jet-surface interaction noise data⁷ and/or used with jet-surface interaction noise prediction schemes, the link between these flow properties and the character of the jet-surface interaction noise may be studied.

The flow field near the surface was systematically mapped to ensure quality data in the primary jet mixing layer, secondary mixing layer, and in the near edge regions. First, PIV flow data were acquired in the streamwise plane to quantify jet spread, velocity, and turbulence levels downstream of the surface in the secondary mixing layer. Streamwise data were also acquired near the nozzle exit and along the length of the surface for surface positions very near the jet to quantify any changes to the primary jet mixing layer. These data were then acquired for all surface lengths and positions in the region near the surface trailing edge. Finally, 3-component cross-stream PIV data were acquired downstream of the surface to provide a more complete image of the flow in the near edge region (e.g. wetted area, turbulence across the edge, etc.) and the development of the secondary shear layer. Note that cross-stream data could not be acquired along the surface because there was not an effective way to suppress reflection of the laser light off the surface without affecting the flow.

II. Test Setup and Data Systems

II.A. Test Setup

The initial jet-surface interaction tests were conducted using the Small Hot Jet Acoustic Rig (SHJAR) located in the Aero-Acoustic Propulsion Laboratory (AAPL) at the NASA Glenn Research Center. The SHJAR is capable of supplying air at flow rates up to 2.7 kg/s to a single-stream nozzle. A hydrogen burning combustor is used to simulate core exhaust at temperatures up to 975 K. Flow conditioning and a line-of-sight muffler are used to achieve a clean and quiet flow at jet exit Mach numbers down to $M_a = 0.35$. Additional information on the SHJAR, including performance validation data, can be found in Ref. 7,8. A round convergent nozzle with a 50.8 mm exit diameter (SMC000) was used for these tests (figure 1(a)).

An additional test was conducted to investigate and validate some significant findings from the first series of tests. The High Flow Jet Exit Rig (HFJER), also located in the AAPL, was used for these experiments. Capable of simulating single, dual, and separate flow nozzle systems with air mass flow rates up to 14 kg/s at temperatures up to 1050 K, the HFJER was used in single stream mode to most closely match the single stream configuration of the SHJAR. More information on the HFJER is available in Ref. 9. A round convergent nozzle with a 50.8 mm exit diameter (TCON) was used for the HFJER portion of the test (figure 1(b)).

Engine exhaust is the primary noise source at take-off conditions where both subsonic and supersonic aircraft operate using similar velocities and flight profiles. Therefore, the jet-surface interaction noise data acquired focused on jet exit velocities between $0.5 \leq M_a \leq 0.9$ to cover the range expected for all airport operations.⁶ The flow data narrows the focus to an approximate take-off condition, $M_a = 0.9$, with static temperature ratio ($T_{s,j}/T_a$) varying from unheated to $T_{s,j}/T_a = 2.27$. Table 1 provides a complete list of the subsonic jet conditions used for these tests. To ensure the correct operating conditions, each operating point, as defined by a Mach number and temperature ratio (for the heated jets), was entered into a facility data acquisition system, which monitored all relevant rig temperatures and pressures once per second to compute the L2-norm difference between the current and specified jet exit conditions. The jet condition was required to be within 0.5% of the specified value throughout the acquisition for an acoustic point to be accepted. The facility data acquisition system also acquired and stored the ambient conditions for later reference and data corrections.

Figure 2(a) shows that the configuration used for these tests was formed using a flat plate near the round nozzle. The plate was articulated by an automated traverse between $0.5 \leq h/D_j \leq 5$ in the radial direction. Three surfaces ($x_{TE}/D_j = 6, 10, 15$) were assembled, each using a single piece of 12.7 mm thick aluminum plate. The downstream edge of each surface was beveled to a 45° angle. In addition to the physical dimensions, the surface introduces additional flow features, such as a wall boundary layer or secondary shear layer, that are not present in an isolated jet (figure 2(b)) but which are important considerations for the noise created. Using both these physical and flow dimensions for normalizing the axial dimensions, the surface positions tested at the unheated jet condition are shown in table 2. Table 3 shows the positions for the heated jet conditions.

Setpoint	NPR P_j/P_a	$T_{s,j}/T_a$	M_a V_{id}/c_a	Mass Flow kg/s	Regime
7	1.860	0.835	0.9	0.90	Subsonic
27	1.360	1.764	0.9	0.43	Subsonic
36	1.273	2.270	0.9	0.33	Subsonic

Table 1. Subsonic jet exit conditions tested.

II.B. Particle Image Velocimetry Data Acquisition and Processing

Particle image velocimetry (PIV) was used to map the velocity field in the jet-surface interaction region and in the flow field downstream of the surface trailing edge. PIV was acquired in two modes: two-component streamwise, and three-component cross-stream. Both used the same lasers, cameras, and image acquisition equipment. Seeding of the jet flow was achieved using 0.4 μm alumina particles, suspended in low-pH alcohol, and sprayed into the flow upstream of the settling chamber of SHJAR. Seeding of the ambient was provided by a pair of MDGTM oil foggers, located in the framework of the SHJAR and directed around the

Setpoint	Nozzle	x_{TE}/D_j	x_{TE}/X_c	0.5	0.55	0.65	0.75	h/D_j	1.0	2.0	3.0	5.0
7	TCON	6	0.86	<i>x</i>	<i>x</i>	<i>x</i>	<i>x</i>	<i>x</i>				
7	SMC000	6	1.02	<i>x</i>				<i>x</i>	<i>x</i>	<i>x</i>	<i>x</i>	
7	SMC000	10	1.69	<i>x</i>				<i>x</i>	<i>x</i>	<i>x</i>	<i>x</i>	
7	SMC000	15	2.54	<i>x</i>				<i>x</i>	<i>x</i>	<i>x</i>	<i>x</i>	

Table 2. Surface lengths and radial positions tested at the unheated jet conditions (setpoint 7 in table 1). Note that radial distances are normalized by jet diameter (h/D_j) while surface lengths are normalized by jet diameter (x_{TE}/D_j) and by potential core length (x_{TE}/X_c) to show where the trailing edge location in both space and relative to the jet flow ($X_c = 5.9D_j$ for SMC000 nozzle with extension, $X_c = 6.95D_j$ for the TCON nozzle).

Setpoint	Nozzle	x_{TE}/D_j	x_{TE}/X_c	0.5	0.5	h/D_j	1.0	2.0	3.0
27	SMC000	6	1.15	<i>x</i>	<i>x</i>	<i>x</i>	<i>x</i>	<i>x</i>	<i>x</i>
36	SMC000	6	1.28	<i>x</i>	<i>x</i>	<i>x</i>	<i>x</i>	<i>x</i>	<i>x</i>

Table 3. Surface lengths and radial positions tested at the hot jet conditions (setpoints 27 and 36 in table 1). Note that radial distances are normalized by jet diameter (h/D_j) while surface lengths are normalized by jet diameter (x_{TE}/D_j) and by potential core length (x_{TE}/X_c) to show where the trailing edge location in both space and relative to the jet flow ($X_c = 5.2D_j$ for setpoint 27 and $X_c = 4.7D_j$ for setpoint 36). Also note that the corresponding unheated point is setpoint 7, SMC000, $x_{TE}/D_j = 6$ in table 2.

jet plume by a pair of 1m-diameter room fans. The PIV system was setup on an automated axial traverse allowing efficient acquisition of multiple planes. The measurement plane was illuminated using a dual head 400 mJ/pulse Nd:YAG laser system. The laser beams were formed into 1 mm by 350 mm light sheets using cylindrical and spherical lenses. The orientation of the light sheet plane was rotated by 90° in order to switch between streamwise and cross-stream PIV configurations. Note that the region around the surface trailing edge was given priority in both arrangements because the jet-surface interaction noise for this configuration is dominated by the trailing edge noise.

A dual side-by-side camera configuration was used to maximize the field of view while maintaining high spatial resolution PIV vector maps. High resolution (4008×2672 pixel) PIV cameras were used with the 4008 pixel axis oriented vertically. The cameras were equipped with 180 mm focal length lenses and positioned so that their fields of view overlapped by 25 mm. Both cameras were connected to a single computer system via a CameraLinkTM PCI card and the 400 frame pair data sequences were acquired and streamed to disk at a rate of 2 frame pairs/camera/second. The two camera views were registered using a grid pattern target with a fiducial mark in the overlapping region of the cameras fields of view. The physical registration of the two cameras was used in the setup of the vector processing grids in the left and right camera images so that no interpolation was required in the merging of the left/right vector maps. The final merged camera vector map covered an area of 308×405 mm. The flow field of interest for most surface lengths could generally be acquired using 4 axial measurement stations. Streamwise PIV was made possible along the plate surface by a small angled groove that was cut along the surface to serve as a beam dump minimizing the amount reflected light reaching the PIV cameras as shown in figure 3. Preliminary noise measurements showed that this groove had minimal effect on the far-field noise and, hence, had negligible effect on the noise generating flow physics.

The Stereo Particle Image Velocimetry (SPIV) system was configured to provide cross-stream measurements of the 3-component velocity field from the test article. The entire SPIV system was mounted on a large traverse system to facilitate performing velocity plane surveys of the flow field. The SPIV system employed two high resolution (4008×2672 pixels) cameras equipped with 180 mm focal length lenses and 8 mm extension tubes to provide a 360×416 mm field of view. The cameras were mounted downstream of the model exit plane at nominally $\pm 45^\circ$ from the nozzle centerline. Seven acquisitions were defined as shown in Table 4. Stereo PIV calibrations were performed using a single plane target translated to 9 axial positions over a ± 2 mm range. A 4th order polynomial was used in the calibration and a calibration verification

operation was employed to insure the calibration overlapped the laser light sheet plane.

Since the AAPL is open to the environment during testing, the SHJAR could not be operated in complete darkness. To accommodate this situation, optical backdrops for the cameras were provided and were offset a suitable distance to minimize any influence on the ambient seeded flow distribution. The frame straddle cameras used in the PIV systems incorporate fast acting shutters in front of the CCD arrays to minimize the duration of the frame-straddled second exposures to nominally 12 ms, down from the camera fixed 240 ms 2nd frame integration period). The complete PIV system, including all cameras and backdrops, data acquisition computers, laser hardware and optics were rigidly mounted on a large axial traverse located downstream of the nozzle exit plane. The travel range of the traverse was approximately 2.5 m, with a positioning accuracy of 1.0 mm.

Velocity vector maps for each camera were computed from the image pairs using the in-house PIVPROC software. The software utilizes conventional multi-pass DPIV cross-correlation processing algorithms and incorporates error detection based on image correlation signal to noise ratio. First pass interrogation region sizes of 64×64 pixels on 32 pixel centers and final pass interrogation region sizes of 32×32 pixels on 16 pixel centers were used to process image pairs from the cameras in both PIV system configurations. For the cross-flow measurement planes near the nozzle, Symmetric Phase Only Filtering (SPOF) was employed to reduce the effects of flare light on the nozzle models directly behind the measurement planes.¹⁰ Without the SPOF processing, images with nozzles illuminated by flare light behind the plane of interest generally produce regions in and around the potential core flow with invalid vector measurements. The SPOF processing technique was not utilized with the axial-flow measurement planes as no images with nozzle models in the background were present. All of the data were processed using LogLut intensity filters and Subregion Distortion processing. Finally, the left/right vector maps combined using an additional in-house code to generate the 3-D vector maps.

While the SPIV system used to capture the cross-stream images provides all three velocity components (u, v, w), the standard PIV system used to acquire the streamwise velocity data only gives the axial and radial components (u, v). Computing the turbulent kinetic energy (TKE) in the cross-stream planes is possible using the simple formula where:

$$TKE = \frac{1}{2}(u^2 + v^2 + w^2) \quad (1)$$

Computing the TKE in the streamwise plane, however, requires assuming that the v and w components of TKE are similar in magnitude such that:

$$TKE = \frac{1}{2}(u^2 + 2v^2) \quad (2)$$

Comparing the estimated TKE in the streamwise plane and the computed TKE in the cross-stream plane supports this assumption in the limited locations acquired using both PIV systems. Nevertheless, this estimation should be noted and used in future comparisons to the data presented.

Acquisition Plane	$x_{PIV}/D_j - x_{TE}/D_j$
1	0.25
2	0.5
3	1.0
4	1.5
5	2.5
6	5.0
7	7.5

Table 4. Location of the cross-stream planes for PIV data acquisition downstream of the trailing edge of the surface.

III. Results

III.A. Unheated Jet Conditions

These PIV data represent the first attempt to measure a jet flow near a surface in the AAPL. Therefore, an isolated jet (no surface) configuration was acquired as a baseline for each nozzle: the SMC000 nozzle with 12" extension^a, the SMC000 nozzle without the extension, and the TCON nozzle. For reference, these data are compared to the Consensus PIV data published by Bridges and Wernet.¹¹ Figure 4 compares the centerline velocity and turbulent kinetic energy (TKE) profiles for each of these configurations normalized by the jet diameter. These results are consistent with the Consensus data for each case except the extended SMC000 nozzle which has shorter potential core ($X_c \approx 5.9$) than measured using the SMC000 nozzle without the extension or the TCON nozzle ($X_c \approx 6.95$). Assuming that the jet-surface interaction noise created at the surface trailing edge is a function of the flow velocity, TKE, and fluctuating pressure in this region, it is reasonable to normalize the axial variable (x) by a flow parameter so that the trailing edge is in a similar position within each jet flow. In this case, normalization by the jet potential core length appears to collapse the centerline velocity and TKE profiles from the measured data with the Consensus data (figure 4). Therefore, all of the jet-surface flow data are presented with the axial variable normalized by the potential core length of the equivalent isolated jet. Furthermore, based on the collapse of the centerline velocity profiles, the Consensus data will be used to represent the isolated flow in each comparison.

The behavior of an isolated jet, for the purpose of validating CFD simulations, is often characterized by the potential core length, determined by the centerline velocity profile, and the turbulent kinetic energy produced and dissipated. A surface near a jet may affect each of these properties depending on its length and position. Mean axial velocity contours acquired at $h/D_j = 1$ using each length surface are shown in figure 6. These figures illustrate qualitatively how the primary jet mixing layer, secondary mixing layer, and wall boundary layer change in size and shape as the surface gets longer. For a more quantitative analysis, data are extracted along the vertical and horizontal lines pictured comparison to other surface positions and to an isolated jet.

Centerline velocity and TKE were extracted from the streamwise PIV data. The shortest surface tested with the SMC000 nozzle, $x_{TE}/D_j = 6$ ($x_{TE}/X_c = 1.02$, figure 7(a)), has very little effect on the centerline velocity profile regardless of radial distance (h/D_j); it does, however, significantly increase the TKE produced when $h/D_j = 0.5$ (figure 7(b)). There is no significant change to either centerline velocity or TKE when $h/D_j \geq 1$. At $x_{TE}/D_j = 10$ ($x_{TE}/X_c = 1.69$), the surface on the nozzle lipline ($h/D_j = 0.5$) creates a small increase in the potential core length followed by a more rapid velocity decay (figure 8(a)) while shifting the peak TKE downstream of the surface trailing edge (figure 8(b)); again, the centerline velocity and TKE profiles are unchanged at $h/D_j \geq 1.0$. This trend continues as the surface becomes longer. When the surface is extended to $x_{TE}/D_j = 15$ ($x_{TE}/X_c = 2.54$), the centerline velocity is higher in the region past the potential core and there is a second peak in the TKE downstream of the surface trailing edge when the surface is at $h/D_j = 0.5$ (figure 9). Unlike the shorter surfaces, there is also some effect on the centerline velocity and TKE at $h/D_j = 1$ when measured with this longest surface.

A surface on one side of a round jet introduces asymmetry into a otherwise symmetric geometry. To investigate these asymmetries, data were extracted along cross-stream lines at several axial stations in the jet plume (as shown in figure 6). The first station extracted from the $x_{TE}/D_j = 6$ data is at $x/X_c = 0.5$ where the velocity cross-stream velocity profile shows this location to still be in the potential core (figure 10(a)). The TKE at $h/D_j = 0.5$ peaks and drops off at $y/D_j = 0.5$ where it encounters the wall boundary layer but otherwise is not greatly altered by the presence of the surface (figure 10(b)). Shortly downstream of the surface trailing edge at $x/X_c = 1.075$, the cross-stream velocity profile at $h/D_j = 0.5$ shows a rapid drop around $y/D_j = 0.5$ indicating the formation of a thin secondary mixing layer (figure 10(c)); the TKE is still lower than in the primary jet mixing layer that is allowed to form when the surface is farther away or the jet is isolated (figure 10(d)). The next velocity profile ($x/X_c = 1.75$) shows development of the secondary mixing layer at $h/D_j = 0.5$, indicated by the more gradual decay (figure 10(e)). The TKE at this station (figure 10(f)) shows a significant increase over the isolated jet levels in both the secondary mixing layer ($y/D_j > 0$) and the primary jet mixing layer ($y/D_j < 0$) when $h/D_j = 0.5$; the TKE does not change noticeably, however, when $h/D_j \geq 1$. Farther downstream at $x/X_c = 2.6$, some asymmetry is still present when $h/D_j = 0.5$ but the velocity and TKE profiles otherwise appear very similar to the fully developed

^aA true isolated case with the extension was not possible due to the set time available so the $x_{TE}/D_j = 6$ surface at $h/D_j = 3$ is used to represent this isolated case. This will be discussed further in Section IV.

isolated jet when $h/D_j \geq 1$ (figures 10(g) and 10(h)).

The $x_{TE}/D_j = 10$ surface extends well past the end of the potential core of the jet when using the extended SMC000 nozzle. This is shown in the cross-stream velocity profiles at $x/X_c = 1.075$ and $x/X_c = 1.750$ (figures 11(a) and 11(c)). This extra length (compared to the $x_{TE}/D_j = 6$ surface) allows the primary jet mixing layer to expand out to the surface, form a wall boundary layer, and subsequently a secondary mixing layer, at both $h/D_j = 0.5$ and $h/D_j = 1$. Farther downstream of the surface trailing edge at $x/X_c = 2.6$, the peak TKE exceeds the level measured in the isolated jet but both the velocity (figure 11(e)) and TKE (figure 11(f)) are biased away from the surface ($y/D_j < 0$) when $h/D_j = 0$. This bias continues in the fully decaying jet measured at $x/X_c = 3.5$. Note that although a secondary mixing appears at $h/D_j = 1$, the flow becomes symmetric downstream of the surface unlike the asymmetric profile that persists at $h/D_j = 0.5$.

Figure 12 shows cross-stream velocity and TKE profiles measured downstream of the trailing edge using the longest surface tested ($x_{TE}/D_j = 15$). At this length, the wall boundary layer and secondary mixing layer that form at $h/D_j = 0.5$ and $h/D_j = 1$ introduce an asymmetry in the velocity and TKE profiles that persist downstream into the decaying jet (figures 12(c) and 12(d)). Furthermore, the velocity and TKE bias away from the surface first observed in the data acquired at $x_{TE}/D_j = 10$ is more pronounced with this longer surface. In particular, note the velocity increase over the isolated jet measured near the jet centerline at $x/X_c = 2.6$ (figure 12(a)) which first appears at $x_{TE}/D_j = 10$ ($x/X_c = 1.75$, figure 11(c)).

The cross-stream TKE and velocity profiles extracted from the streamwise PIV data show that the velocity and TKE are notably affected when the surface is at the nozzle lipline ($h/D_j = 0.5$). Therefore, complete cross-stream PIV images were acquired to provide a more complete view of the flow in this region. Figure 13 shows streamwise contours of the TKE acquired using each surface placed at $h/D_j = 0.5$ (where the surface has the greatest effect). The dashed on each plot indicate the locations where complete cross-stream PIV planes were acquired.

The TKE measured downstream of each surface at $h/D_j = 0.5$ using the cross-stream SPIV system is shown in figure 14. These images confirm the trends observed in the streamwise data; when $x_{TE}/D_j \leq 10$ the secondary mixing layer forms and the peak TKE at each measured plane moves from the primary jet mixing layer (away from the surface) to the secondary mixing layer (downstream of the surface) and the TKE is relatively low throughout the flow downstream of the surface when $x_{TE}/D_j = 15$. Unlike the streamwise data, however, these images allow an estimate of the trailing edge length covered by flow (wetted area) which may be an important consideration for jet-surface interaction noise. At $x_{TE}/D_j = 6$, the flow covers $y/D_j \approx \pm 0.8$ across the surface trailing edge (figure 14(a)). When the surface is longer, the jet spread increases to cover $y/D_j \approx \pm 1$ at $x_{TE}/D_j = 10$ (figure 14(b)) and $y/D_j \approx \pm 1.2$ at $x_{TE}/D_j = 15$ (figure 14(c)).

The PIV data acquired using the SMC000 nozzle showed that the surface at $h/D_j = 0.5$ produced significant changes in the flow and that the affect of the surface on the flow was minimal at $h/D_j = 1$, the next position for which data were acquired. Therefore, additional streamwise PIV data were acquired during a second test entry (using the TCON nozzle) with the $x_{TE}/D_j = 6$ surface moving in smaller increments between $0.5 \leq h/D_j \leq 1$. The TKE measured for each position is shown in figure 15. At $h/D_j = 0.5$ (figure 15(a)), the secondary mixing layer contains the strongest region of TKE in the entire flow which is consistent with the results obtained in the previous test (figure 13(a)). The secondary mixing layer remains the region of peak TKE when the surface is moved slightly off the nozzle lipline ($h/D_j = 0.55$, figure 15(b)). However, when the surface is moved another small increment to $h/D_j = 0.65$ (figure 15(c)), the TKE in the secondary mixing layer is much closer to the levels found in the primary jet mixing layer. At $h/D_j = 0.75$, the TKE in the two mixing layers is almost the same (figure 15(d)). Finally, at $h/D_j = 1$ the TKE in the secondary mixing layer is below the levels found in the primary jet mixing layer confirming the change previously observed when the surface is in this near jet region.

III.B. Hot Jet Conditions

The majority of the flow data accrued during the jet-surface interaction tests used unheated jets. A subset of the jet-surface configurations, consisting of the $x_{TE}/D_j = 6$ surface length at $h/D_j = 0.5$, 1, and 2, were tested using heated jets. These data were intended to provide some insight into the role of heat on the flow in the surface trailing edge region. Figure 16 shows the TKE measured for the $x_{TE}/D_j = 6$ surface at $h/D_j = 0.5$. Like the unheated jet data presented in Section III.A, the axial variable is normalized by the jet potential core length. However, because the different jet temperatures result in different potential core

lengths, the surface trailing edge, which has a fixed physical length, is now in a different location relative to the jet plume. This results in higher TKE levels in the primary jet mixing at surface trailing edge. The secondary mixing layer, however, has its origin fixed at the surface trailing edge and, therefore, is fairly similar independent of jet temperature.

PIV data were acquired for each jet temperature in a cross-stream plane $0.25D_j$ downstream of the surface trailing edge. These data, shown in figure 17, further illustrate how changing the jet temperature changes the TKE in the region around the surface trailing edge; the primary jet mixing layer is much more developed (thicker region of high TKE) at the trailing edge as the jet temperature increases as if these are effectively three different surface lengths. However, the TKE is relatively low in the secondary mixing layer that is just beginning to form in each case.

Finally, the centerline velocity and TKE measured at each jet temperature are shown in figure 18). When the jet is heated, both the velocity and TKE profiles collapse very well over the first $2.5X_c$. However, there are some minor differences when the data from these heated jets are compared to the unheated jet. This appears consistent with data showing that a jet variables change quickly with the first addition of heat and then more gradually when additional heat is added.¹¹

IV. Analysis

The data presented in Section III provide an insight into the behavior of a jet exhaust when placed near a surface. Using the assumption that velocity, TKE, and wetted trailing edge length are the most important parameters governing the production of jet-surface interaction noise, the data acquired were shown at locations relative to the jet potential core length. This normalization was shown to reasonably collapse the velocity and TKE profiles when the correct potential core length was used for each jet. However, the extension used in the jet-surface interaction test to provide clearance between an upstream contraction and the surface significantly changed the potential core length in the isolated jet (figure 4). Preliminary boundary layer measurements conducted using a hot wire probe have shown that the boundary layer at the nozzle exit is much thicker when the extension is used. Furthermore, the laminar versus turbulent character of the boundary layer changes when the extension is added. Both of these factors may contribute to the overall shortening of the potential core observed (e.g. Refs. 14,15). Nevertheless, the data appear to be consistent across the two jet-surface tests presented and with the isolated Consensus dataset once normalized by the measured potential core length (figure 5).

When the surface is very close to the nozzle lipline, the peak TKE appears in the secondary mixing layer downstream of the surface trailing edge. Furthermore, a relationship between the secondary mixing layer and primary jet mixing layer appears in certain configurations where the TKE is amplified in both regions (e.g. figure 10(f)) as if the secondary mixing layer excites the flow in the downstream primary jet mixing layer. The source of this increase is not well explained in the current dataset; it may be an unsteady phenomenon that could be captured by time averaged measurements. This increase in TKE in both mixing layers represents an important finding as many jet mixing noise prediction methods are based on some integration of the TKE. However, phased-array source localization measurements have not shown a dominant source in this region;⁴ This does not necessarily imply that the jet mixing noise does not increase due to the higher TKE only that it may not be the dominant noise source in these configurations (the phased-array shows the surface trailing edge noise as dominant).

The streamwise and cross-stream flow data consistently show that a surface must be very near the nozzle lipline to have a significant and lasting effect on the flow downstream of the surface. This is best demonstrated in figure 15 where the peak TKE is generated in the secondary mixing layer at $h/D_j = 0.5$ but decreases to levels below those found in the primary jet mixing layer by $h/D_j = 1$. As might be expected, longer surfaces cause larger and more lasting changes to the flow. However, even the longest surface tested ($x_{TE}/D_j = 15$) had a relatively minor effect on the flow at $h/D_j = 1$ and almost no effect for $h/D_j \geq 2$ (figure 12). Thus, these data indicate that only surfaces very close to the jet lipline impact the velocity and TKE near the surface trailing edge. However, surfaces in this near jet region appear to be the most likely in actual aircraft applications where it may not be practical for efficiency and control reasons to place all surface farther away.

While the PIV data acquired shows that the velocity and TKE near the surface trailing edge are only affected by the presence of a surface when it is quite close to the nozzle lipline, the corresponding far-field noise data showed the spectral characteristics of jet-surface interaction noise present when the surface was significantly farther away ($h/D_j > 1$ in many cases).⁶ For example, the PIV flow data shows minimal effect

of a surface at $x_{TE}/D_j = 6$, $h/D_j = 2$, as indicated by comparison to the isolated jet in figure 10(c), but there is a significant increase in far-field noise data consistent with jet-surface interaction noise. Thus, it appears that the surface only needs to be subject to the pressure fluctuations in the hydrodynamic region that surrounds a high-speed jet flow to generate some level of jet-surface interaction noise. This is an important finding for jet-surface noise prediction work, particularly those methods based on computation fluid dynamics, because it implies that it may not enough to just get the mean flow variables correct in order to successfully predict the jet-surface interaction noise; prediction schemes that rely on pressure fluctuations at the trailing edge (e.g. Amiet's method¹⁶) may have an advantage when considering these configurations.

Finally, these data show the possible difficulties normalizing the spatial variables around a heated jet near a surface. As the potential core becomes shorter with the addition of heat, the surface becomes, effectively, longer relative to the primary jet mixing layer. However, as the secondary jet mixing layer, by definition, can not form until the surface trailing edge, it is still linked to the physical distance between the nozzle exit and the surface trailing edge. Thus, the normalization used by a given prediction scheme will depend on the source (or effect) being modeled; a model for the noise shielding effect may normalize by potential core length to best capture the extent of the jet covered while a model for the mixing noise itself may normalize by the jet diameter to better capture the primary jet and secondary mixing layers.

V. Conclusions

Many engine exhaust noise prediction methods lack the capability to include nearby airframe surfaces in the prediction. Understanding how the exhaust flow changes near these surfaces, however, will allow researchers to develop, improve, and validate better noise prediction schemes that consider the affects of the airframe. Velocity data have been acquired using streamwise and cross-stream PIV systems over a range of surface positions and jet conditions. These flow data complement previously published far-field noise measurements. An analysis of these data has shown:

- (1) Only surface very near the jet lipline ($h/D_j < 1$) create significant and lasting effects on the flow farther downstream.
- (1) Surfaces near the jet lipline create a region of high turbulent kinetic energy in the secondary jet mixing layer downstream of the surface trailing edge that may exceed the level found in the primary jet mixing layer.
- (3) Jet-surface interaction noise is created as long as the the surface is within the hydrodynamic pressure region of the jet, not just within the high-speed flow region.

A subset of the total noise and flow data base has been presented to a few of the more important results. These data, when combined with the far-field noise data, form a solid database for developing and validating noise prediction methods that include airframe surfaces near the engine exhaust.

Acknowledgements

This work was supported by the NASA Fundamental Aeronautics Program, High Speed and Fixed Wing Projects.

References

- ¹Kim, H.D., "Distributed Propulsion Vehicles", ICAS 2010.
- ²Welge, H.R., Bonet, J., Magee, T., Tompkins, D., Britt, T.R., Nelson, C., Miller, G., Stenson, D., Staubach, J.B., Bala, N., Duge, R., O'Brien, M., Cedoz, R., Barlow, A., Martens, S., Viars, P., Rasheed, A., Kirby, M., Raczynski, C., Roughen, K., Doyle, S., Alston, K., Page, J., and Plotkin, K.J., "N+3 Advanced Concept Studies for Supersonic Commercial Transport Aircraft Entering Service in the 2030-2035 Period", NASA/CR-2011-217084, 2011.
- ³Brown, C.A. , "Jet-Surface Interaction Test: Far-Field Noise Results", J. Eng. Gas Turbines Power, **135**(7), Jun. 2013.
- ⁴Podboy, G., "Jet-Surface Interaction Test: Phased Array Noise Source Localization Results", ASME GT2012-69801, 2012.
- ⁵Gruschka, H. D. and Schrecker, G. O., "Aeroacoustic Characteristics of Jet Flap Type Exhausts", AIAA 72-0130, 1972.
- ⁶Brown, C., "Developing an Empirical Model for Jet-Surface Interaction Noise", AIAA 2014-0878, 2014.
- ⁷Brown, C. and Bridges, J., "Small Hot Jet Acoustic Rig Validation", NASA/TM-2006-214324, 2006.

- ⁸Bridges, J. and Brown, C., "Validation of the Small Hot Jet Acoustic Rig for Jet Noise Research", AIAA 2005-2846, 2005.
- ⁹Brown, C., Henderson, B., and Bridges, J., "Data Quality Assurance for Supersonic Jet Noise Measurements", ASME GT2010-22545, 2010.
- ¹⁰Wernet, M.P., "Symmetric Phase Only Filtering: a New Paradigm for DPIV Data Processing", Meas. Sci. Technology, **16**, pp. 601-618, 2005.
- ¹¹Bridges, J. and Wernet, Mark P., 2011, "The NASA Subsonic Jet Particle Image Velocimetry (PIV) Dataset", NASA/TM-2011-216807.
- ¹²Witze, P.O., "Centerline velocity decay of compressible free jets", AIAA J. **12**(4), pp. 417-418, 1974.
- ¹³Bridges, James, "Noise from Aft Deck Exhaust Nozzles - Differences in Experimental Embodiments", AIAA 2014-0876, 2014.
- ¹⁴Zaman, K.B.M.Q., "Effect of Initial Boundary-Layer State on Subsonic Jet Noise", AIAA J. **50**(8), pp. 1784-1795, August 2012.
- ¹⁵Bogey, C. and Bailly, C., "Influence of nozzle-exit boundary-layer conditions on the flow and acoustic fields of initially laminar jets", J. Fluid Mech. **663**, pp. 507-538, 2010.
- ¹⁶Amiet, R.K., "Noise due to a turbulent flow past a trailing edge", J. of Sound and Vib., **47**(3), pp. 387-393, 1976.

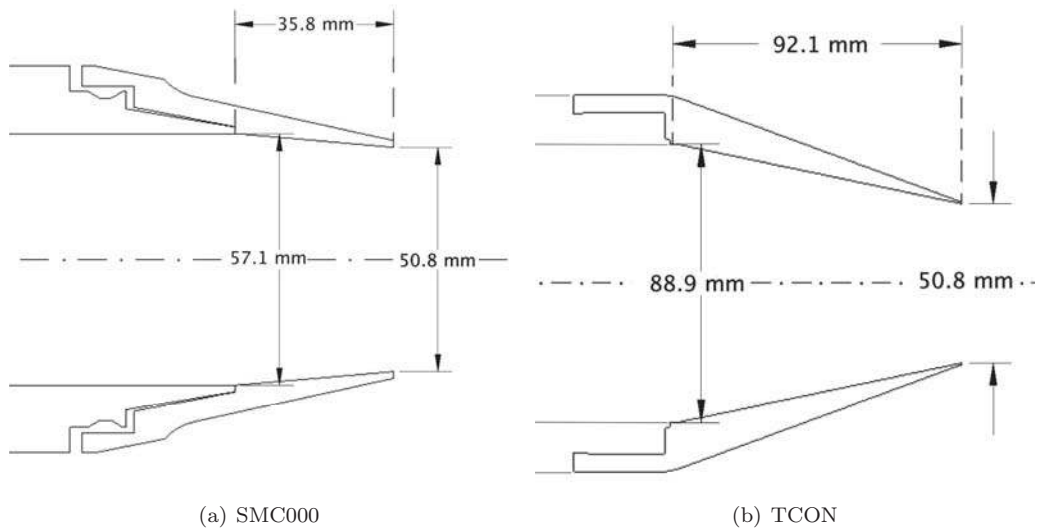


Figure 1. Schematic showing the internal flow line of the SMC000 and TCON nozzles tested.

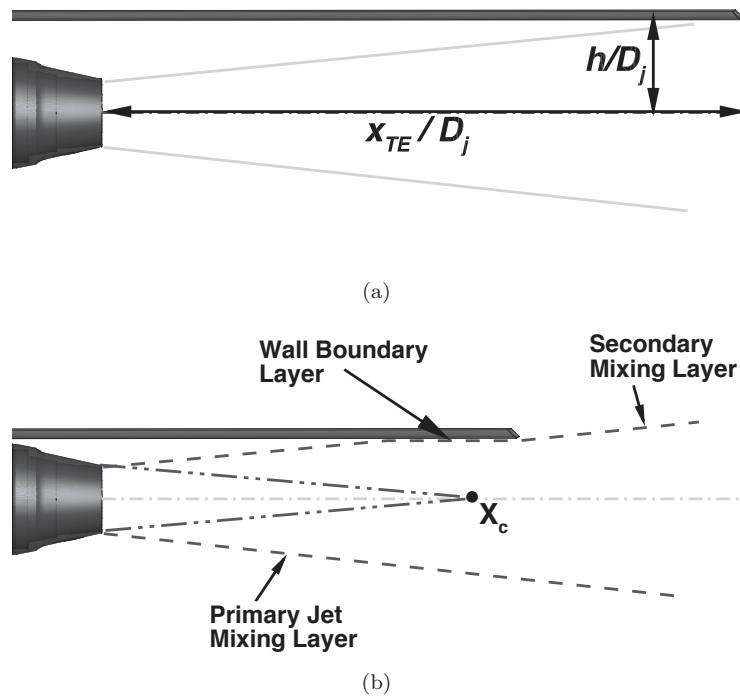


Figure 2. Schematics showing the nomenclature used to describe the surface position (a) and showing the nomenclature used to describe the flow regions (b).

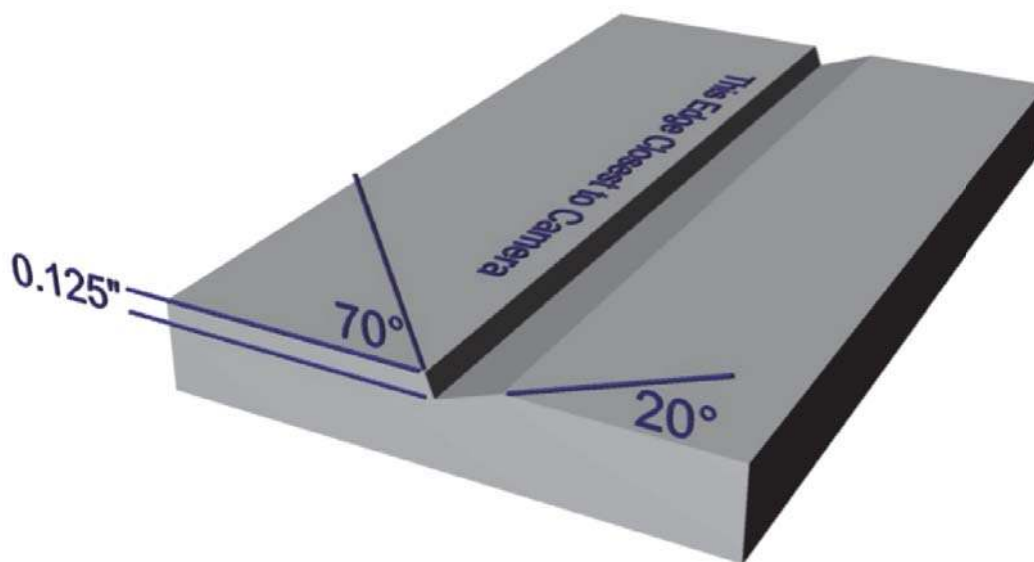


Figure 3. Drawing showing the the axial beam dump groove cut into the surface to prevent the scattering of the PIV laser light.

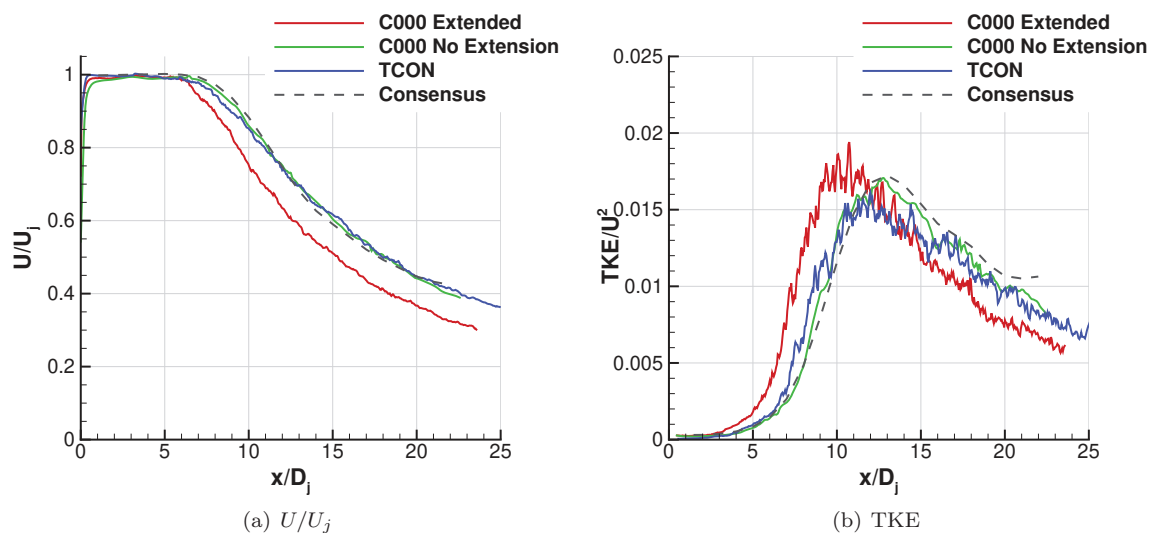


Figure 4. Centerline axial velocity and turbulent kinetic energy (TKE) for isolated jets normalized by jet diameter (x/D_j).

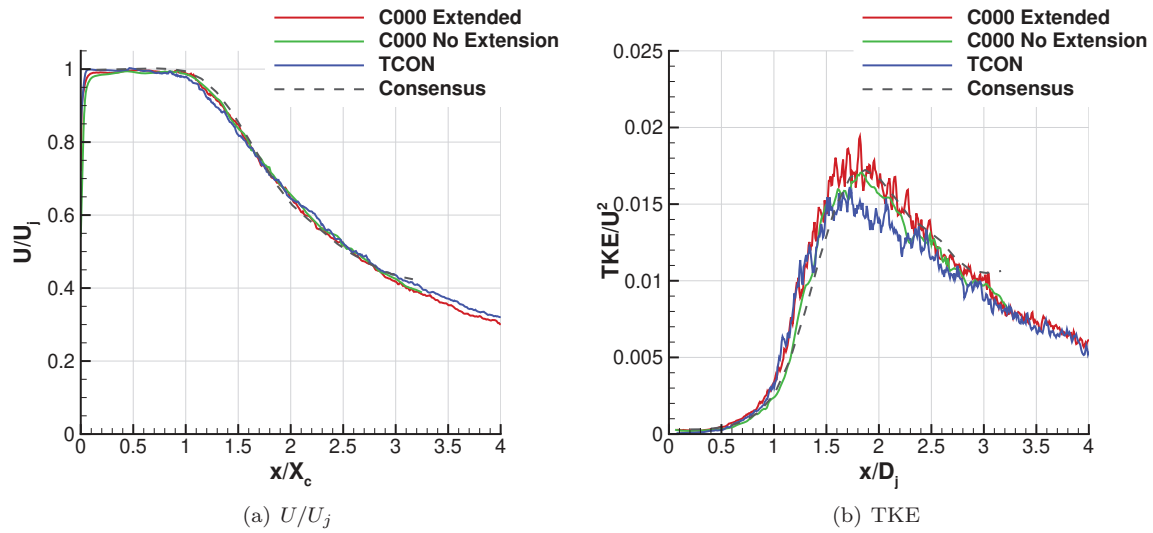


Figure 5. Centerline turbulent kinetic energy (TKE) for isolated jets normalized by jet diameter (x/D_j) and potential core length (x/X_c).

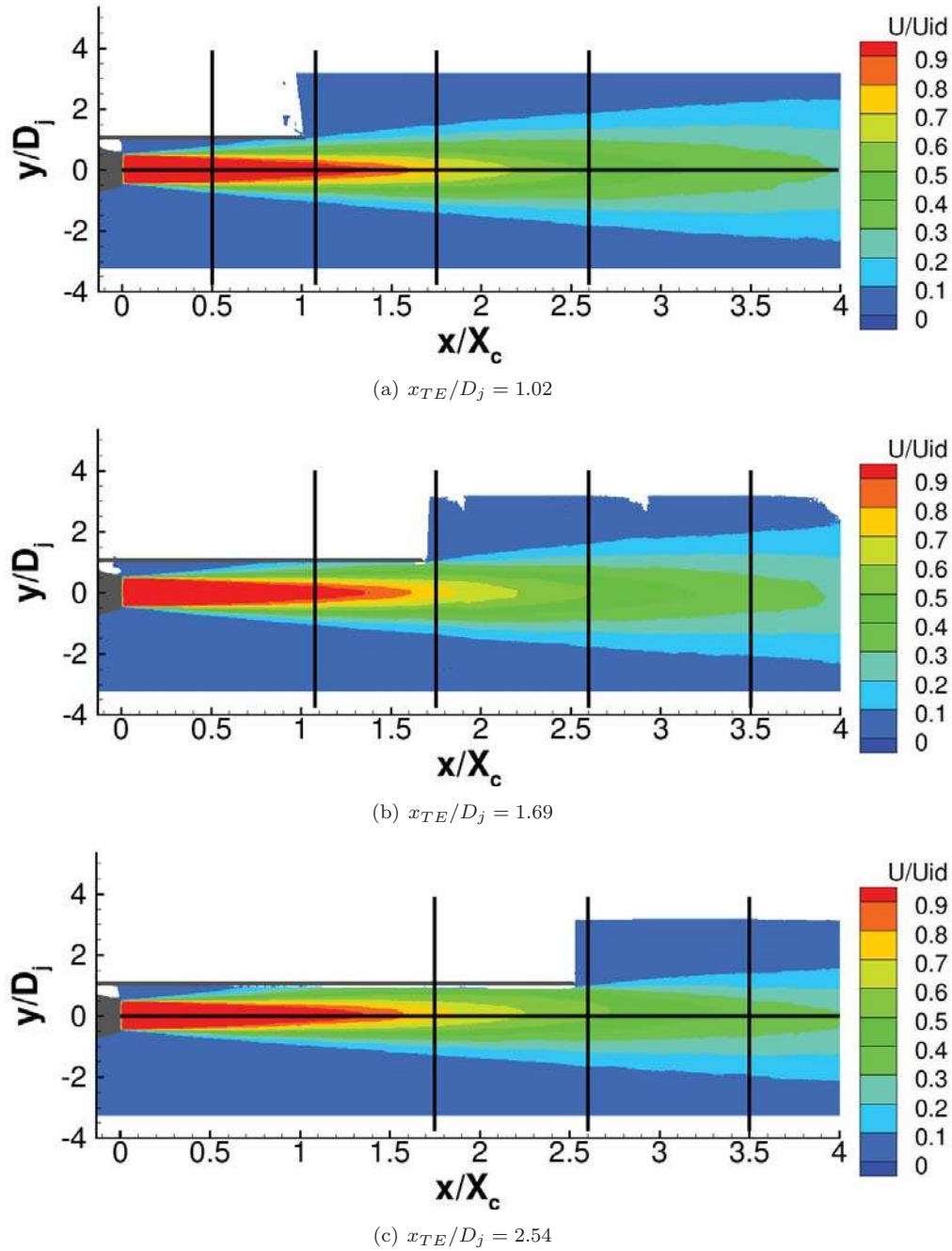


Figure 6. Mean axial velocity acquired at setpoint 7, SMC000 nozzle, and $h/D_j = 1.0$ using the $x_{TE}/D_j = 6$ (top, (a)), $x_{TE}/D_j = 10$ (middle, (b)), and $x_{TE}/D_j = 15$ (bottom, (c)) surfaces. Note that the horizontal and vertical black lines indicate locations where data have been extracted for comparison and analysis.

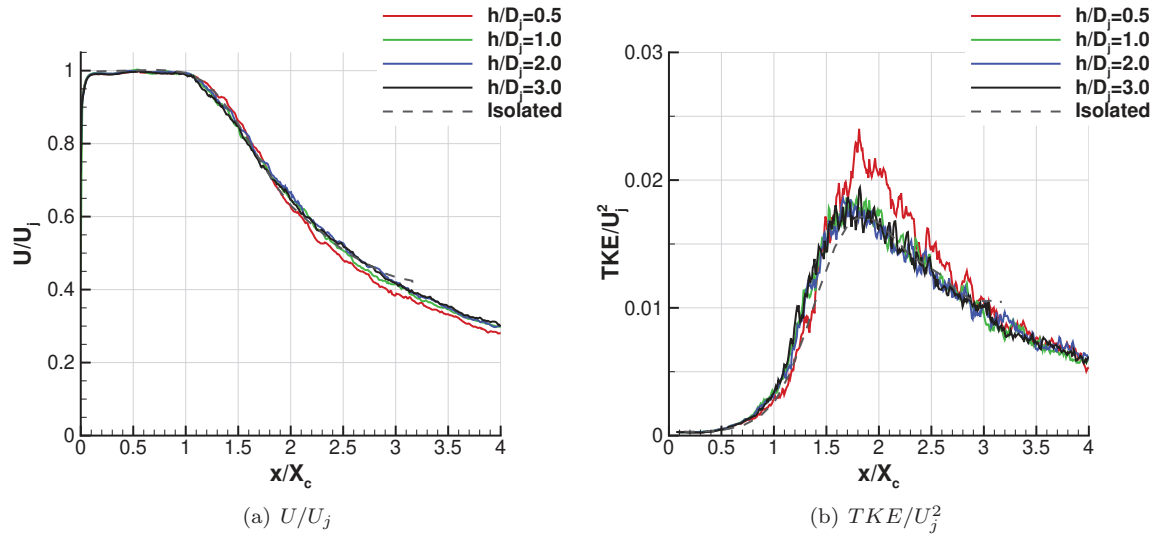


Figure 7. Centerline axial velocity and TKE measured at setpoint 7, SMC000 nozzle, with surface $x_{TE}/D_j = 6$ ($x_{TE}/X_c = 1.02$).

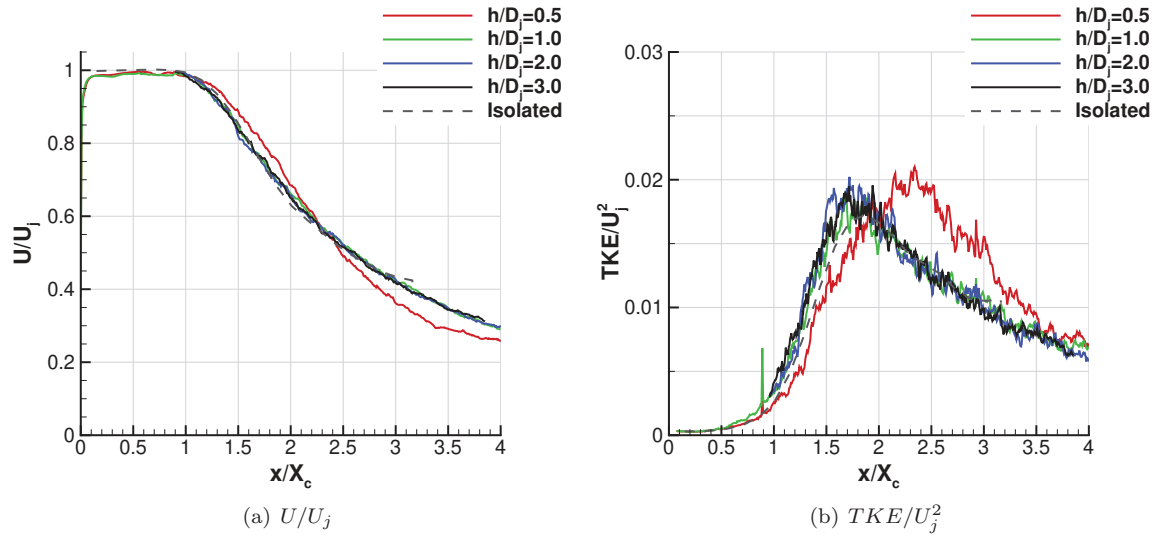


Figure 8. Centerline axial velocity and TKE measured at setpoint 7, SMC000 nozzle, with surface $x_{TE}/D_j = 10$ ($x_{TE}/X_c = 1.69$).

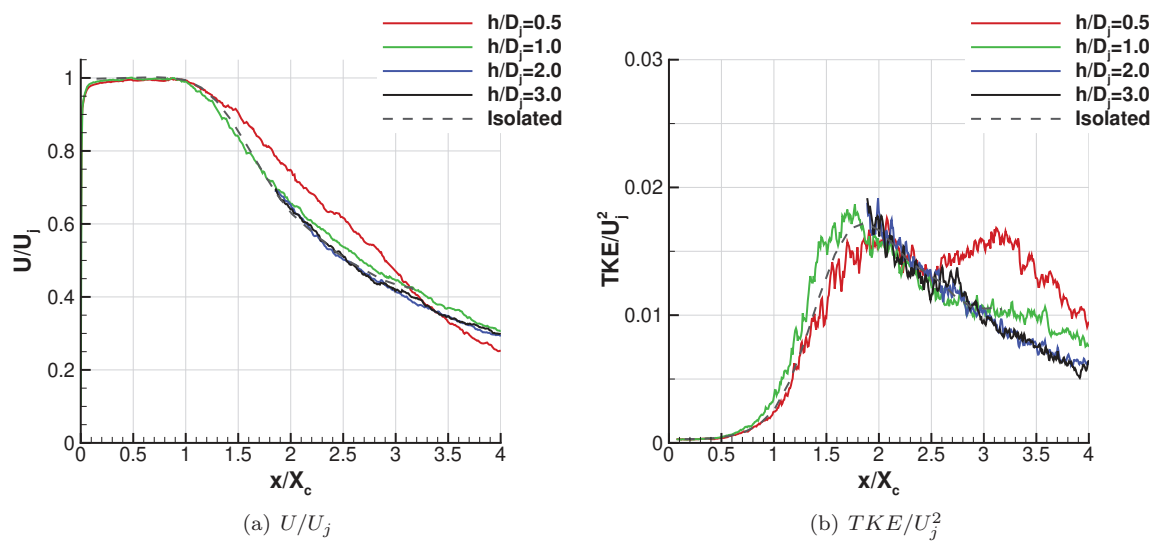


Figure 9. Axial velocity and TKE on the jet centerline measured at setpoint 7, SMC000 nozzle, with surface $x_{TE}/D_j = 15$ ($x_{TE}/X_c = 2.54$).

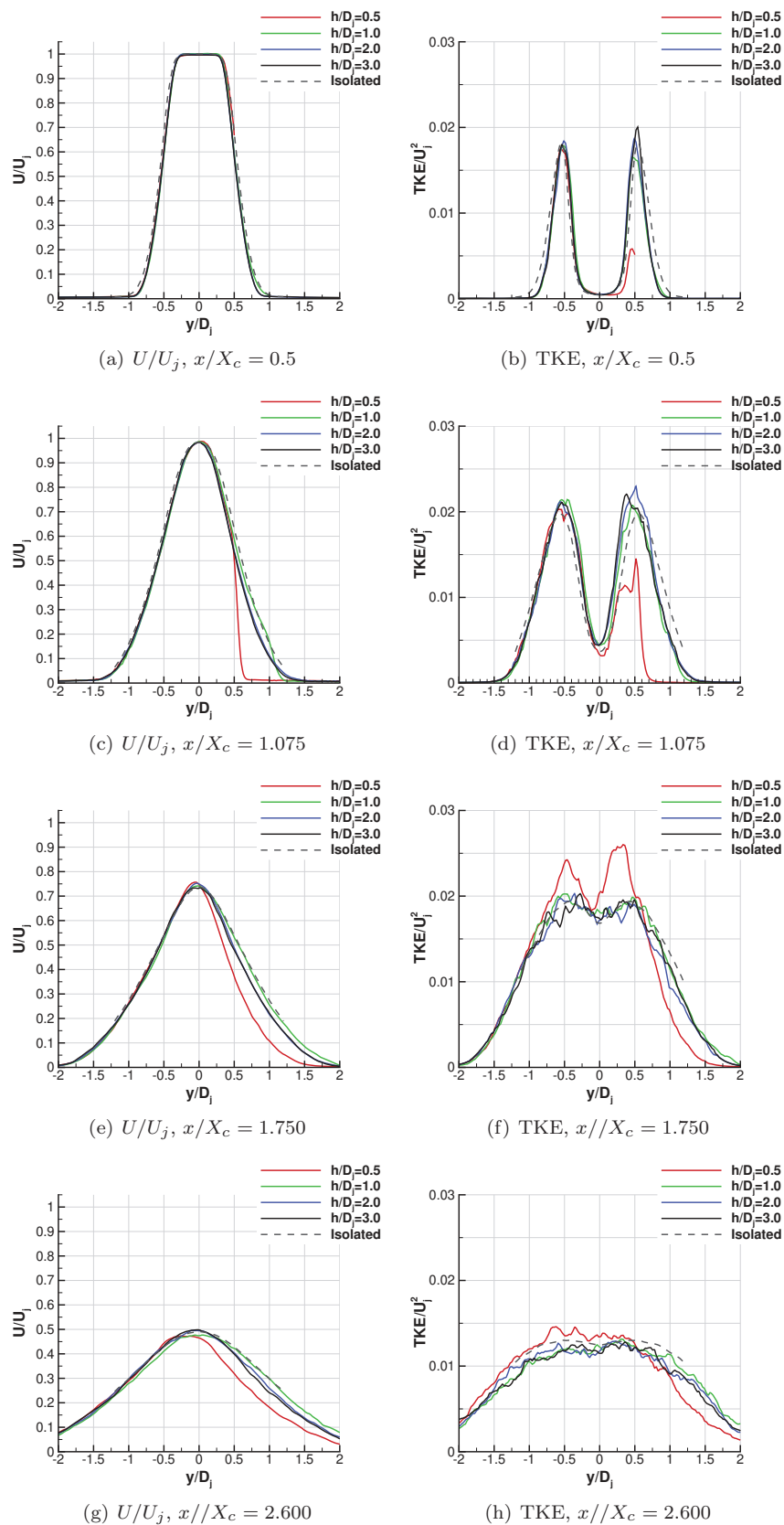


Figure 10. Axial velocity (left) and TKE (right) at 4 axial stations measured using the SMC000 nozzle and the $x_{TE}/D_j = 6$ ($x_{TE}/X_c = 1.02$) surface for setpoint 7.

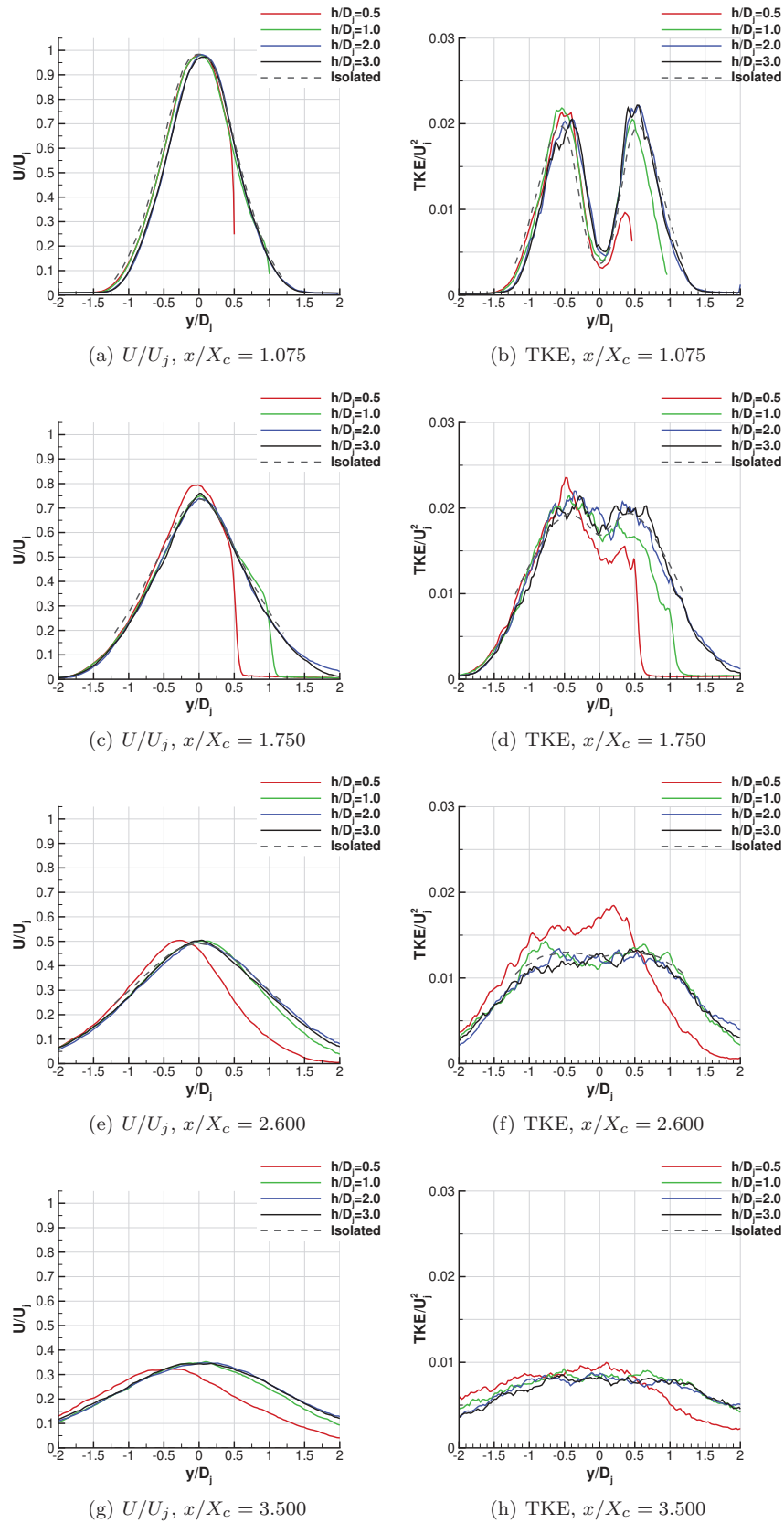


Figure 11. Axial velocity (left) and TKE (right) at 4 axial stations measured using the SMC000 nozzle and the $x_{TE}/D_j = 10$ ($x_{TE}/X_c = 1.69$) surface for setpoint 7.

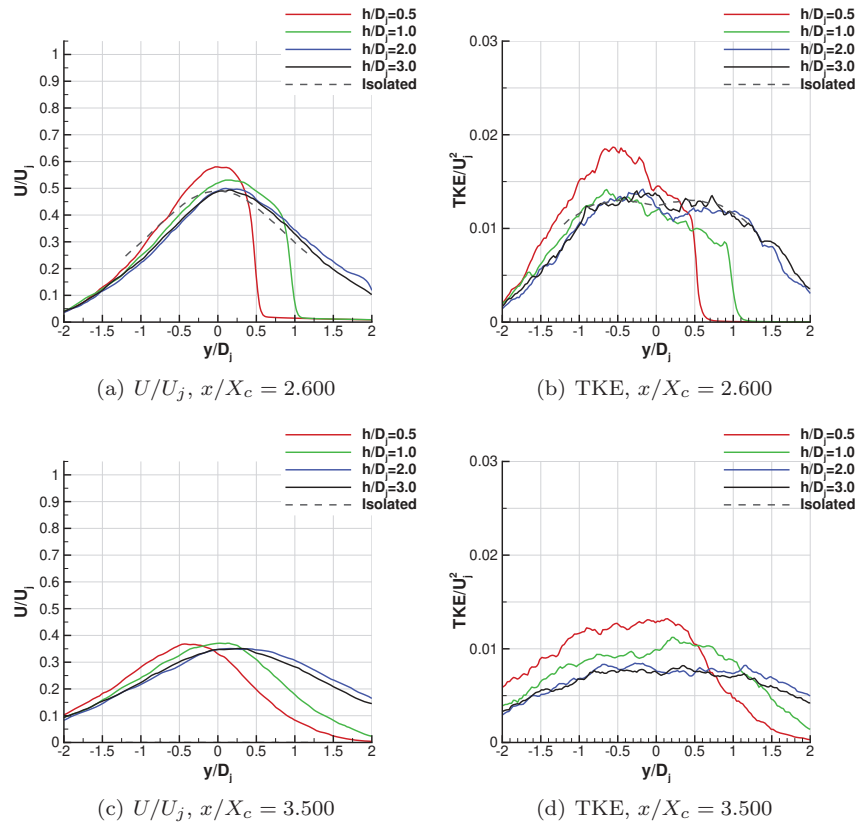


Figure 12. Axial velocity (left) and TKE (right) at 4 axial stations measured using the SMC000 nozzle and the $x_{TE}/D_j = 15$ ($x_{TE}/X_c = 2.54$) surface for setpoint 7.

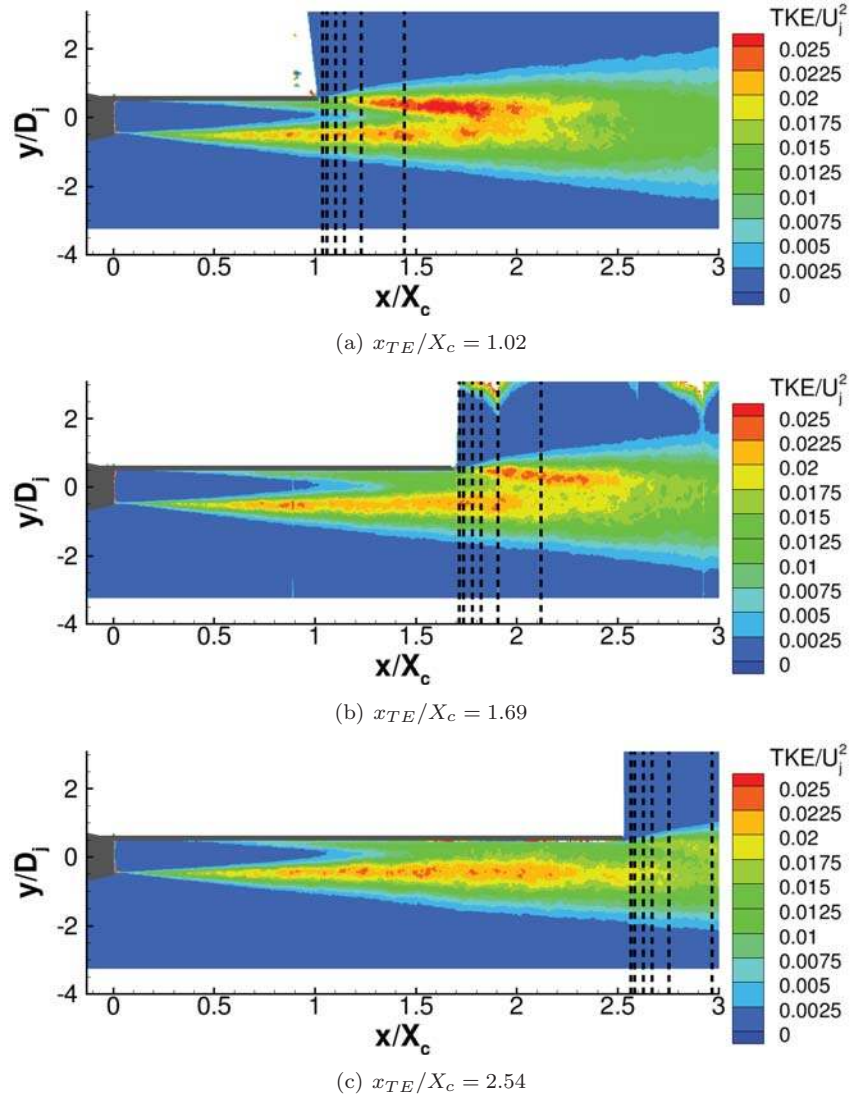


Figure 13. TKE acquired at setpoint 7 using the SMC000 nozzle with the $x_{TE}/D_j = 6$ (top, (a)), $x_{TE}/D_j = 10$ (middle, (b)), and $x_{TE}/D_j = 15$ (bottom, (c)) surfaces at $h/D_j = 0.5$. Note that the dashed black lines indicate locations where cross-stream PIV images shown in figure 14 were acquired.

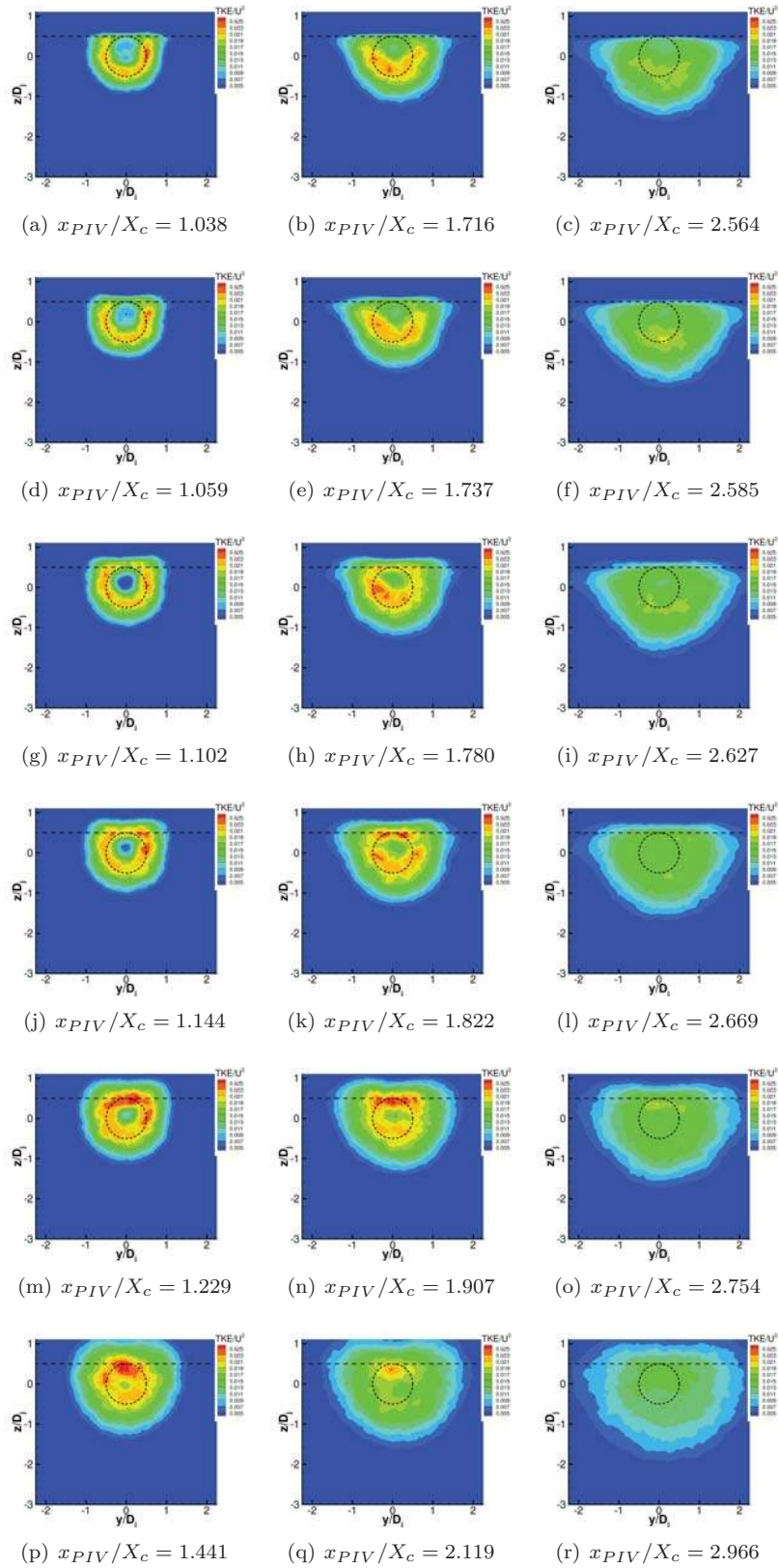


Figure 14. TKE acquired at setpoint 7 using the SMC000 nozzle with surface lengths $x_{TE}/D_j = 6$ (left), $x_{TE}/D_j = 10$ (center) and $x_{TE}/D_j = 15$ (right) all at $h/D_j = 0.5$. Note that the dashed lines represent the surface trailing edge and the nozzle lip locations. and that each row of plots is at a constant distance from the surface trailing edge.

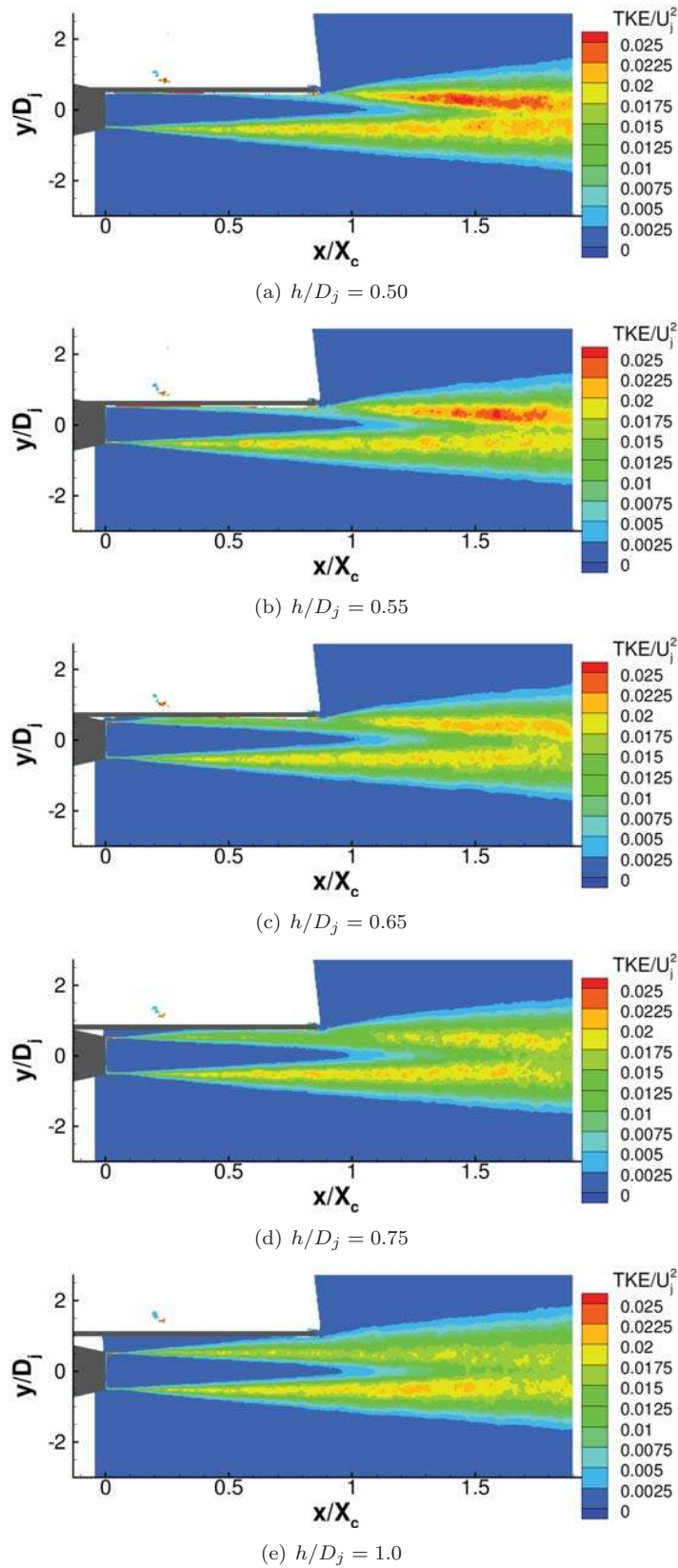


Figure 15. TKE acquired at setpoint 7 using the TCON nozzle with the $x_{TE}/D_j = 6$ surface at $h/D_j = 0.5$ (top, (a)), $h/D_j = 0.55$ (b), $h/D_j = 0.65$ (c), $h/D_j = 0.75$ (d), $h/D_j = 1.0$ (bottom, (e)).

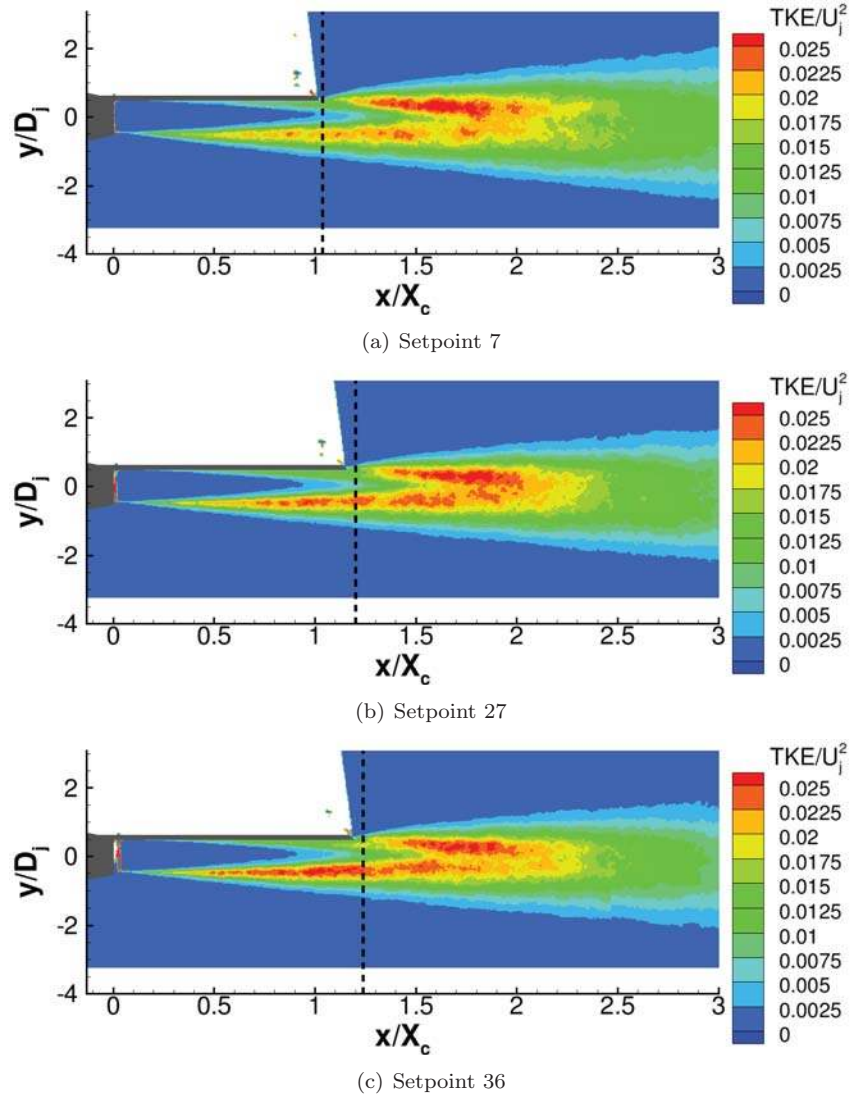


Figure 16. Mean axial velocity acquired at setpoints 7, 27, and 36 (SMC000 nozzle) and with a $x_{TE}/D_j = 6$ surface length placed at $h/D_j = 0.5$.

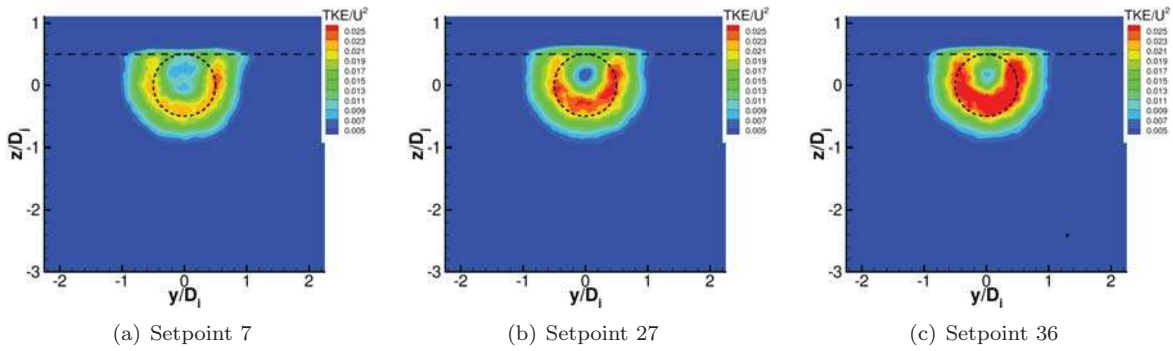


Figure 17. TKE measured at $x_{PIV}/D_j = 6.25$, setpoint 7, SMC000 nozzle, with a surface at $x_{TE}/D_j = 6$, $h/D_j = 0.5$.

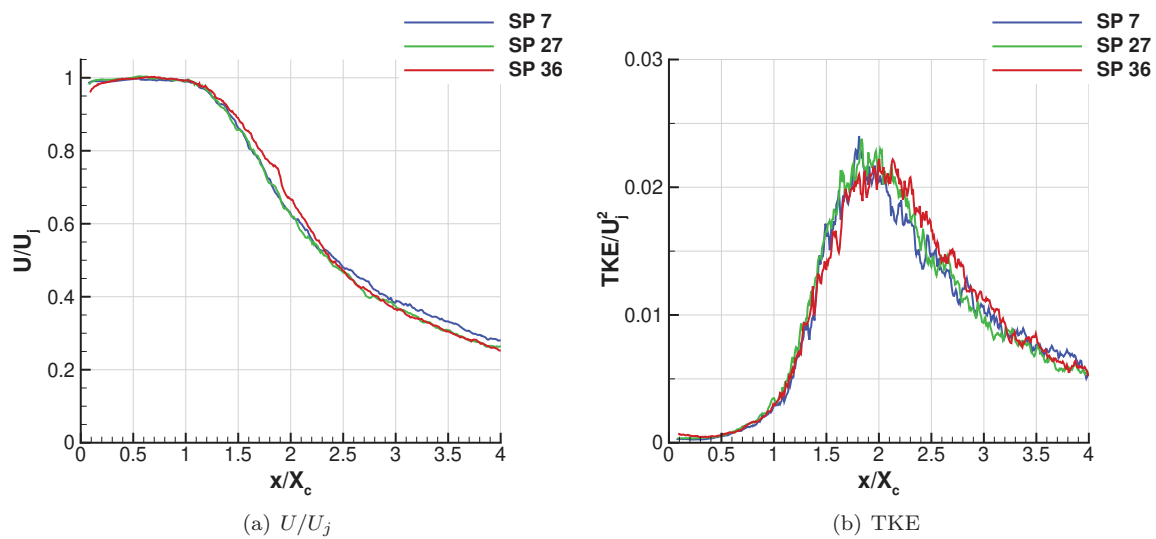


Figure 18. Axial velocity and TKE on the jet centerline measured at setpoint 7, SMC000 nozzle, with surface $x_{TE}/D_j = 6$ at $h/D_j = 0.5$.